In Situ Observations of the Microphysical Properties of Wave, Cirrus, and Anvil Clouds. Part II: Cirrus Clouds

R. PAUL LAWSON, BRAD BAKER, BRYAN PILSON, AND QIXU MO

SPEC Inc., Boulder, Colorado

(Manuscript received 31 January 2005, in final form 7 March 2006)

ABSTRACT

A Learjet research aircraft was used to collect microphysical data, including cloud particle imager (CPI) measurements of ice particle size and shape, in 22 midlatitude cirrus clouds. The dataset was collected while the aircraft flew 104 horizontal legs, totaling over 15 000 km in clouds. Cloud temperatures ranged from −28° to −61°C.

The measurements show that cirrus particle size distributions are mostly bimodal, displaying a maximum in number concentration, area, and mass near 30 μm and another smaller maximum near 200–300 μm. CPI images show that particles with rosette shapes, which include mixed-habit rosettes and platelike polycrystals, constitute over 50% of the surface area and mass of ice particles >50 μm in cirrus clouds. Approximately 40% of the remaining mass of ice particles >50 μm are found in irregular shapes, with a few percent each in columns and spheroidal shapes. Plates account for <1% of the total mass. Particles <50 μm account for 99% of the total number concentration, 69% of the shortwave extinction, and 40% of the mass in midlatitude cirrus. Plots and average equations for area versus particle size are shown for various particle habits, and can be used in studies involving radiative transfer.

The average particle concentration in midlatitude cirrus is on the order of 1 cm^{-3} with occasional 10-km averages exceeding 5 cm^{-3}. There is a strong similarity of microphysical properties of ice particles between wave clouds and cirrus clouds, suggesting that, like wave clouds, cirrus ice particles first experience conversion to liquid water and/or solution drops before freezing.

1. Introduction

The size, shape, and concentration of ice crystals in cirrus clouds have a major impact on the earth's radiation budget. For example, Liou (1986) showed that cirrus particles play an important role in the energy balance of the earth–atmosphere system through their interactions with solar and terrestrial radiation. Stephens et al. (1990) concluded that the prediction of cirrus cloud feedback on climate is limited by our lack of understanding of the relationship between the size and shape of ice crystals, and the gross radiative properties of cirrus. Labonnote et al. (2000) determined that accurate measurements of the size and shape of cirrus particles were essential to obtain reliable inversion products from remote observations. Kristjánsson et al. (2000) used climate models to show that the treatment of ice particle size and habit may have a significant impact on climate change.

Before the development of the cloud particle imager (CPI) in 1997 (Lawson et al. 2001), detailed shapes of airborne measurements of ice particles were available from "impactor" and "replicator" devices that collected the ice crystals on slides, or made Formvar (plastic) replicas (e.g., Heymsfield 1973; Miloshevich and Heymsfield 1997; Arnott et al. 1994). While providing fine detail of some small ice particles, overall, impactor data are generally very challenging to interpret due to the breakup of particles larger than approximately 200 μm, contamination, and overlapping particles on the medium (Arnott et al. 1994). Breakup can be minimized by flying the impactor on a balloon or incorporating the impactor device into a decelerator. Cooper and Vali (1981) successfully exposed oil-coated slides in a decelerator, but the resulting data collection rates are very low.

Most of the previous digital data collected in cirrus have been recorded using the Particle Measuring Sys-

Corresponding author address: R. Paul Lawson, SPEC Inc., Suite 200, 3022 Sterling Circle, Boulder, CO 80301.
E-mail: plawson@specinc.com

© 2006 American Meteorological Society

tems (PMS) 2D-C (cloud) optical array probe (Knollenberg 1970, 1981). However, the detailed shapes of particles $<\sim 300$ μm are not discernable, and crystal details, such as riming, side planes, etc., are ambiguous.

Heymsfield and Platt (1984) examined replicator data collected in cirrus and determined that the predominant crystal types in the temperature range from $-20°$ to $-40°$C were "spatial" (or polycrystalline) forms, with some columns, plates, and bullets. In the temperature range from $-40°$ to $-50°$C, they found predominantly hollow columns. At temperatures below $-50°$C, they observed predominantly hollow and solid columns, with some hexagonal plates and thick plates. They note that, although observed infrequently, bullet rosettes were sometimes found. However, based on the replicator images shown in Heymsfield and Platt (1984), the "spatial" polycrystalline crystals shown in the $-40°$ to $-50°$C temperature range would likely be classified in this work as rosette-shaped ice crystals.

Recent investigations in cirrus using a CPI (e.g., Lawson et al. 2001; Sassen et al. 2001; Heymsfield et al. 2002) suggest that midlatitude and high-latitude cirrus may contain more rosette-shaped crystals than previously reported. In this paper we present CPI image data that show that the majority of the mass in the 22 cirrus clouds investigated in this study comprises rosette-shaped ice crystals.

Little is known about the physical processes associated with the formation of cirrus clouds. Laboratory investigations have shown that polycrystalline ice crystals form when a supercooled drop freezes rapidly (Pruppacher and Klett 1997; Bacon et al. 2003). Bailey and Hallett (2004) recently performed a detailed laboratory study showing that platelike polycrystals form in the temperature range from $-20°$ to $-40°$C and mixed-habit rosettes from $-25°$ to $-40°$C. They also found that "pristine rosettes" (i.e., rosette shapes that are not mixed habit and are without platelike and side-plane features) only form at temperatures below $-40°$C. Since mixed-habit, platelike, and rosette polycrystals all have a rosette shape (the dictionary definition of rosette is a "small rose"), we refer to the general term "rosette shape" to include mixed-habit rosettes and all polycrystals with a rose shape. In addition, some of the figures in this paper simply refer to "rosettes," and this should always be interpreted to mean rosette shapes.

The lowest temperature at which supercooled liquid water is typically observed in clouds is approximately $-37°$C (e.g., Heymsfield and Miloshevich 1993; Baker and Lawson 2006a, hereafter Part I). Because polycrystalline ice crystals can form when a liquid drop freezes quickly, it is possible that rosette-shaped ice crystals found in cirrus at temperatures below $-37°$C result from the freezing of tiny solution drops (i.e., a deliquesced aerosol). Recent cloud chamber investigations (Field et al. 2004; Cotton et al. 2004) suggest that there may be two separate nucleation events occurring. The first nucleation event at $\sim 105\%$ relative humidity with respect to ice is thought to be deposition ice nucleation. The second nucleation event could be explained by homogeneous freezing at hydrophilic sites on the deliquesced aerosol. However, the actual process of nucleation in cirrus cloud remains uncertain at this time. A significant reason for our lack of understanding of the physical processes contributing to the formation of cirrus ice particles is the difficulty of observing cirrus formation in situ. Unlike ice particles in cumulus and wave clouds, cirrus do not have an obvious formation stage, and therefore it is not possible to reliably position a research aircraft in the development stage of cirrus clouds.

In this paper we show the results of analyzing CPI and other cloud microphysical measurements collected in 22 cirrus clouds. This is the largest cirrus dataset analyzed to date that includes CPI measurements. We show average particle size distributions (PSDs), particle concentration, ice water content (IWC), extinction coefficient, effective radius, equivalent radar reflectivity, histograms of particle habits, and plots of particle areas versus particle lengths. A comparison of these results is compared with data collected in wave clouds presented in Part I. We show the similarities in PSDs and particle types in wave and cirrus clouds and discuss possible explanations for physical commonalities in ice crystal formation and growth in these clouds. The results presented here can be used in radiation studies and also to assist in the understanding of physical processes simulated in cloud models.

2. Data collection

Microphysical measurements were collected in cirrus clouds by the SPEC Learjet research aircraft on 22 days over a period of five years. The Learjet flew 104 horizontal legs in cirrus clouds totaling a distance of more than 15 000 km. Here, we briefly summarize the relevant cloud microphysical instrumentation and refer the reader to Part I for a more detailed description. Cloud particles were measured using a PMS forward scattering spectrometer probe (FSSP) (Knollenberg 1981) with electronics upgraded by Droplet Measurement Technologies (DMT), a 2D-C optical imaging probe, and a SPEC CPI. Composite PSDs are generated by combining measurements from the FSSP, CPI, and 2D-C probes using techniques described in Lawson et al. (2001) and Part I. Various microphysical param-

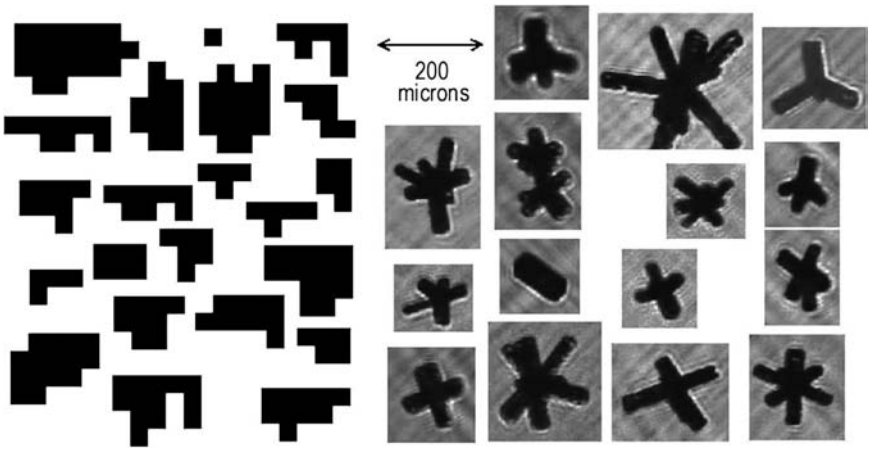

FIG. 1. Examples of particle images observed by (left) the PMS 2D-C probe and (right) the CPI in a cirrus cloud investigated on 20 October 2001. The two probes were both located on the SPEC Learjet research aircraft and the image data were recorded simultaneously.

eters are computed from the particle data, including total particle concentration, IWC, effective particle radius, extinction coefficient, and radar reflectivity.

IWC is computed using an improved algorithm described by Baker and Lawson (2006b) that incorporates image length, width, area, and perimeter into a combined single parameter that has a power law relationship to particle mass. Baker and Lawson (2006b) report a 50% rms error reduction in particle mass estimation using the new technique compared with the Mitchell et al. (1990) techniques. However, because there is no airborne standard for measuring particle mass, it is not possible to quantitatively estimate the error in IWC from 2D particle imagery. Therefore, errors in IWC determination from 2D particle imagery may (or may not) be large, but there is no way to reliably estimate the uncertainty. Also, the Baker and Lawson (2006b) analysis was based on the Mitchell et al. (1990) dataset that was collected at the surface in the Sierra Nevada, and this dataset may not be representative of crystal types found in cirrus clouds. Ice particle mass was also measured using a Nevzorov total water content probe, which measures IWC in glaciated clouds (Korolev et al. 1998b). Particle habits are determined by software that automatically classifies CPI images. The automatic classification is qualified by visually classifying a representative subset of the CPI images. This process is discussed in more detail in section 3a.

For the past three decades, aircraft measurements of the size and shape of ice crystals in cirrus clouds have relied mostly on the PMS optical array probes developed in the 1970s. However, laboratory and wind tunnel investigations by Korolev et al. (1991, 1998a) and Strapp et al. (2001), and recent comparisons with a new imaging probe (Lawson et al. 2006b), show that the large majority of particles with diameters less than about 150 μm are poorly sized and often missed all together by these optical array probes. Results from the research reported in this paper show that particles with maximum dimensions from about 10 to 75 μm contain the majority of the surface area and mass in cirrus clouds. As shown in Fig. 1, the relatively course (effective) pixel size of the older optical array probes renders only scant details of crystal shape for particles with sizes $<\sim$300 μm. Development of the CPI has facilitated the collection of high-resolution digital images of ice particles (Fig. 1) as they pass "on the fly" through the instrument. Particles are imaged with 2.3-μm pixel resolution and 256 gray levels, providing more detailed and accurate information on the size and shape of ice crystals (Lawson et al. 2001; Part I).

There has been some question regarding the significance of ice particle clustering and crystal shattering on the inlets of particle probes, and how this affects measurements of small ice particle concentrations, especially measurements made by the FSSP. Field et al. (2003) and Gayet et al. (2002) present the most recent summary of possible effects of crystal shattering on FSSP concentration measurements. Field et al. show measurements that suggest that clustering of ice particles in cirrus may be the result of shattering of crystals $>\sim$350 μm. The data are inconclusive as to the contribution of shattering to total particle concentration, but even when suspected effects of shattering (i.e., clustering) are removed, ice concentrations from $\sim$0.2 to 1 cm^{-3} are still observed in cirrus, which is one to two orders of magnitude higher than most previous measurements (e.g., Heymsfield and Platt 1984; Dowling

TABLE 1. Cloud-base and cloud-top altitude, temperature, duration in cloud, and cloud location for cirrus clouds investigated by the SPEC Learjet (FL × 100 = pressure altitude in ft).

Date	Cloud base	Cloud top	Temperature (°C)	Duration in cloud (h)	Cloud location
16 Nov 1998	FL 250	FL 390	−28 to −50	3	Utah
1 Jun 1999	FL 300	FL 350	−39 to −51	1.25	Utah
1 Mar 2000	FL 245	FL 300	−31 to −39	1.5	Oklahoma
19 Oct 2000	FL 330	FL 350	−48 to −50	1	Utah
1 Dec 2000	FL 370	FL 390	−57 to −63	1.5	Utah
1 May 2001	FL 290	FL 350	−34 to −53	1	Utah
9 May 2001	FL 290	FL 330	−40 to −51	1	Colorado
25 May 2001	FL 330	FL 370	−51 to −59	1	Colorado
30 Oct 2001	FL 280	FL 350	−33 to −49	1	Colorado
31 Oct 2001	FL 290	FL 310	−37 to −40	1	Nebraska
7 Nov 2001	FL 290	FL 350	−37 to −50	1.5	Colorado
12 Nov 2001	FL 310	FL 370	−44 to −58	1.25	Utah
14 Nov 2001	FL 330	FL 350	−50 to −54	0.5	Texas
21 Nov 2001	FL 320	FL 350	−46 to −55	0.75	Colorado
13 Nov 2002	FL 330	FL 370	−48 to −54	0.75	Oklahoma
19 Nov 2002	FL 260	FL 290	−32 to −43	1	Oklahoma
22 Nov 2002	FL 330	FL 350	−48 to −51	1.25	Colorado
23 Nov 2002	FL 310	FL 340	−43 to −50	1.25	Oklahoma
29 Oct 2003	FL 380	FL 400	−56 to −61	0.75	Wyoming
12 Nov 2003	FL 290	FL 390	−37 to −59	1.5	Colorado
17 Nov 2003	FL 240	FL 290	−33 to −44	1	Colorado
24 Nov 2003	FL 240	FL 350	−32 to −57	1	Wyoming
Total missions	Cloud-base range	Cloud-top range	Max temperature range	Total duration (h), Number of legs, distance in cloud (km)	
22	FL 240–FL 370	FL 290–FL 400	−28° to −61°C	28.25, 104, 15 000	

and Radke 1990; Heymsfield and Miloshevich 1995, hereafter HM95). Gayet et al. (2002) show measurements in synoptically generated cirrus where up to 5 cm^{-3} of ice is measured when there are no particles larger than 100 μm, a particle size that is unlikely to contribute significantly to particle shattering. Lawson et al. (2001) show an example of CPI images where there is clustering of small ice particles and average concentrations >1 cm^{-3} in an arctic cirrus cloud, but the possibility of crystal shattering was not considered in this case. Particle clustering is considered again in section 3b, which also contains an example of FSSP, CPI, and 2D-C and Nevzorov probe data where particle concentrations are from 3 to 8 cm^{-3} in cirrus, and there are no ice particles >100 μm.

Table 1 shows the date, cloud-base altitude and temperature, cloud-top altitude and temperature, and the duration in cloud for the 22 flights in cirrus clouds investigated by the SPEC Learjet over Utah, Colorado, and Oklahoma. The cirrus were all synoptically generated, not remnants of convection. Since the locations—Utah, Colorado, Wyoming, and Oklahoma—are downwind of major mountain ranges, some of the cirrus may have been orographically enhanced, but this is difficult to quantify. Most of the clouds investigated were cirrus clouds with thin to moderate vertical depths ($<\sim$2 km), except for three cases (16 November 1998, 12 November 2003, 24 November 2003), where the cloud depth exceeded 3 km (Table 1).

The cloud-base and cloud-top temperatures were determined by average aircraft temperature measurements when the Learjet flew just above cloud base and when it skimmed cloud top. The average duration of a horizontal leg in a cirrus cloud, including course reversal, was about 16 minutes. Generally, cloud-base altitude was measured or estimated on climb out and cloud top was measured on the first cloud pass. The remaining cloud penetrations were then planned to be evenly spaced between cloud bottom and cloud top. The number of horizontal legs per mission can be estimated in Table 1 by dividing the duration in cloud, shown in hours, by 0.27 h. Using this estimate, it can be seen that most of the clouds were sampled throughout their depth at 1000-ft ($\sim$300 m) increments, while a few clouds benefited from repeated sampling at an altitude, and a few of the clouds were sampled at 2000-ft ($\sim$600 m) increments. Thus, for the most part, clouds in the entire dataset were sampled throughout the entire cloud depth in 1000- or 2000-ft increments. Occasionally, Air Traffic Control (ATC) restrictions limited ac-

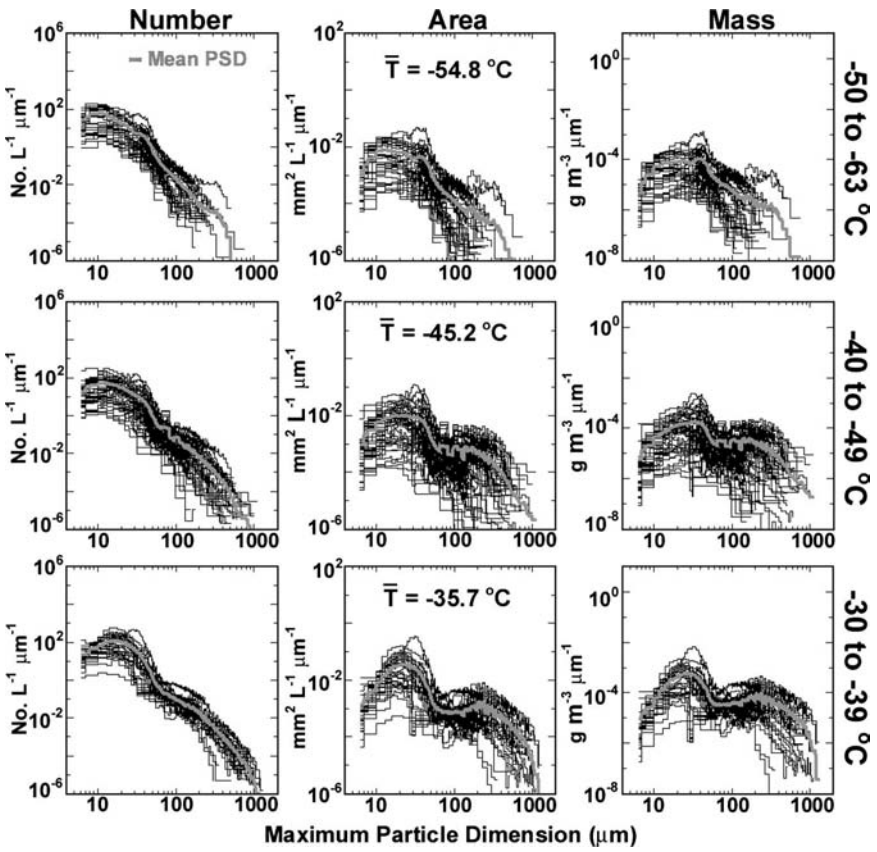

FIG. 2. Number, area, and mass particle size distributions for three temperature ranges based on 22 Learjet flights in over 15 000 km of cirrus clouds. See text for explanation of how PSDs are generated.

cess to certain altitudes, but this was generally resolved during the course of the flight, or has been noted in the discussion presented in this paper.

3. Microphysics

a. Average microphysical properties

The PSDs, averaged over each of the 104 legs flown in 22 cirrus clouds, are shown in Fig. 2. The distributions are segregated according to temperature and are shown based on particle number concentration, area, and mass. The mean of each temperature-segregated group is also shown. The PSDs were derived by combining measurements from an FSSP, CPI, and 2D-C. The technique used is similar to that described in Lawson et al. (2001). The CPI PSD is scaled to the 2D-C PSD in the 200–300-μm size range, where the 2D-C PSD measurements are considered to be most reliable. In cases where the particles are too small to be imaged by the 2D-C, the CPI total particle concentration is adjusted so that the FSSP and CPI PSDs overlap in the 20–40-μm size range. The CPI PSD was adjusted for the reduced probability of detecting smaller particles. This affects particles smaller than approximately 100 μm. The probability of detection was assumed to be proportional to the particle area as measured from the image. The constant of proportionality was fixed by a comparison with FSSP data.

Table 2 shows averages, standard deviations, minimum and maximum values of particle concentration, effective radius, extinction coefficient, IWC, and equivalent radar reflectivity for the three temperature zones. Effective radius is computed using the technique described for r_{eff_B} in Part I. The PSDs in the two warmer temperature regions in Fig. 2 are strongly bimodal with a peak (particularly evident in the area and mass PSDs) in the small particle region (near 30 μm), and a lesser maximum near the 200–300-μm size regime. PSDs in cirrus with bimodal shapes have been reported by HM95, Ivanova et al. (2001), and by Part I for wave clouds. The average PSD in the coldest ($-50°$ to $-61°$C) region shows only a hint of being bimodal. One possible explanation for the bimodality is the shattering of large crystals on the inlet of the FSSP (Field et

TABLE 2. Means, standard deviations, and extreme values of microphysical properties derived from Learjet data collected in the 22 cirrus clouds shown in Table 1. The measurements are separated into three temperature zones and N is the number of legs flown in each temperature zone.

	Mean	Std dev	Max	Min
		−50° to −63°C (N = 36)		
IWC (g m^{-3})	0.005	0.007	0.035	0.001
Concentration (L^{-1})	846	853	3679	36
Extinction (km^{-1})	0.464	0.585	3.00	0.023
R_{eff} (μm)	15.4	4.7	26.0	8.1
Radar reflectivity (dBZ)	−27.5	−21.6	−13.8	−51.6
		−40° to −49°C (N = 49)		
IWC (g m^{-3})	0.013	0.017	0.077	0.001
Concentration (L^{-1})	968	951	3817	30
Extinction (km^{-1})	0.920	1.060	4.779	.017
R_{eff} (μm)	21.53	7.10	41.46	9.99
Radar reflectivity (dBZ)	−21.13	−18.59	−11	−53.5
		−30° to −39°C (N = 30)		
IWC (g m^{-3})	0.037	0.038	0.125	0.002
Concentration (L^{-1})	2170	2159	8267	81
Extinction (km^{-1})	2.404	2.663	11.094	0.140
R_{eff} (μm)	26.5	7.5	43.1	13.0
Radar reflectivity (dBZ)	−15.5	−14.8	−8.8	−39.1

al. 2003). However, the bimodal PSDs reported by HM95 are based on measurements in cirrus from −24° to −44°C using a balloonborne replicator, which does not induce crystal shattering.

Another distinct trend in the PSDs is the increase in particle size with decreasing altitude and higher temperatures. Kajikawa and Heymsfield (1989) report that aggregates dominate the large end of the PSD in deep synoptically generated cirrus. Heymsfield et al. (2002) show examples of CPI images of aggregates in the lower regions of a deep cirrus cloud. We have also observed cirrus cases where aggregation of rosette-shaped ice particles was obvious and very significant lower in cirrus clouds (see Sassen et al. 2001); however, aggregation does not always occur and appears to be much less frequent than in other clouds, such as the outflow region of continental thunderstorms (Connolly et al. 2005). While we did not perform a quantitative analysis of aggregation, we have found that it is sometimes difficult to distinguish aggregation from complex diffusional growth patterns. These complex shapes appear to develop as ice particles fall through different temperature regimes in deep cirrus clouds, producing side planes and appendages with various habit characteristics. The diffusional growth of these complex crystals may be augmented by aggregation. We show examples of ice particles in deep cirrus later in this section.

Figure 3 shows bar plots of particle habits recognized by software that automatically sorts particles >50 μm into six habit categories. In this case, only the particles imaged by the CPI are analyzed and the number of particles in each category is not adjusted for detection sensitivity. This has the effect of underweighting particles smaller than approximately 100 μm in addition to ignoring particles smaller than 50 μm. Again, as mentioned in the introduction, "rosettes" in this figure refer to rosette-shaped ice particles.

Figure 3 also shows examples of typical CPI images placed into each category, including images that may be misclassified by the software. The software used to automatically classify the particle habits was checked manually to obtain an estimate of its accuracy. Sections of each flight leg were selected at random and an average of approximately 25% of all particles >50 μm in each section were classified manually. The results are shown in the caption of Fig. 3. Totaling all particle habits together, approximately 12% of the particles were misclassified according to human eye. The largest percentage (27%) misclassified was in the plate category but, as shown in Fig. 3, plates only account for approximately 1% of the total number of ice particles. More importantly, rosette-shaped images are classified correctly almost 90% of the time. We separate budding rosettes as having short, stubby branches and interpret these to be small rosette-shaped particles. We distinguish growing crystals from sublimating crystals based on the work of Korolev and Isaac (2004), who show that sublimating CPI images typically have very rounded edges. Some regions of the cirrus clouds investigated (7 of the 104 legs) had distinct regions with virtually no small particles and only irregular, rounded shapes with sizes that ranged from 100 to 200 μm in size. Some

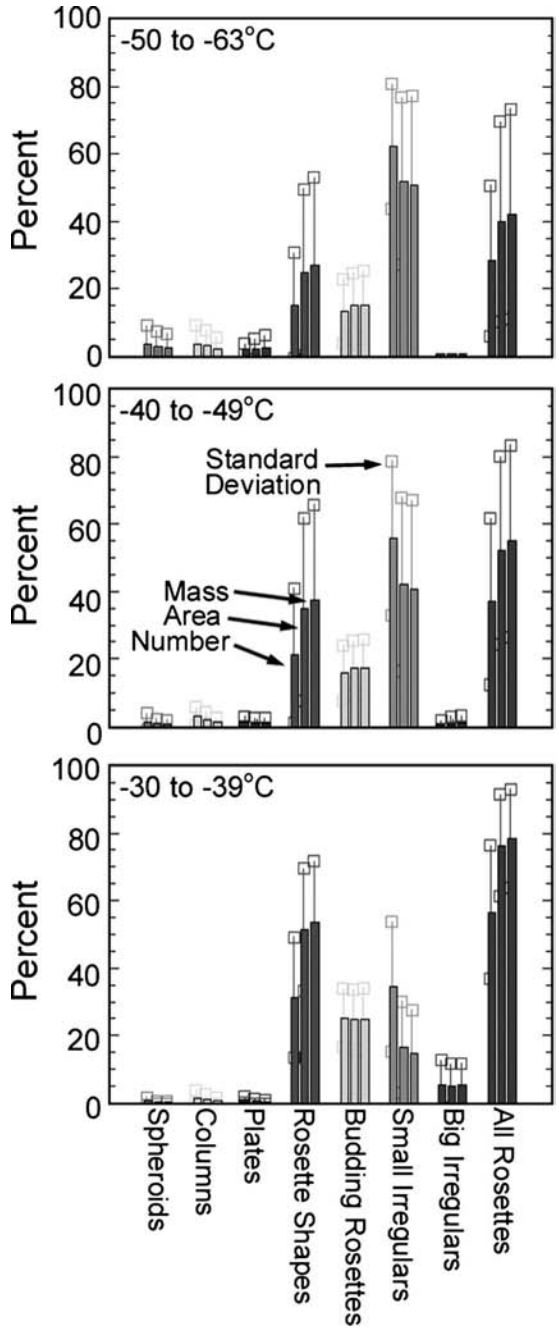

FIG. 3. Histogram showing the results of automatic particle habit classification as a function of number, area, and mass for three temperature ranges. Data were collected during 104 Learjet legs in cirrus. Standard deviation is not an error estimate, but instead shows the leg-to-leg variability in particle habit distributions. When compared to a manual classification, the following discrepancies in the automatic method were found, spheroids: 5%; columns: 8%; plates: 27%; budding rosettes: 20%; rosette shapes: 11%; small irregulars: 11%; and large irregulars: 13%. Total for all categories: 12%

examples are shown in the small irregular category in Fig. 4. We interpret these regions as being composed almost entirely of sublimating ice particles. Except for plates, which were almost nonexistent, the most significant discrepancy (20%) between the automatic and manual classifications shown in the caption of Fig. 3 occurs for budding rosettes. Budding rosettes were sometimes classified as small irregulars and vice versa. This is because the distinction of particle types in these two categories is often unclear and subjective, as shown in the examples of images in Fig. 4.

The results shown in Fig. 3 indicate that rosette shapes are the predominately recognizable particle shape in cirrus clouds. However, there is also consistency in our cirrus CPI particle image observations and observations found in the literature that report rosette shapes in the temperature range from −20° to about −55°C. That is, rosette-shaped ice particles observed from about −20° to −40°C in wave clouds (Part I), ice crystals precipitating at the South Pole (Ohtake and Inoue 1980; Lawson et al. 2006a), and CPI images of ice particles in cirrus (reported here) are consistent in the finding that the rosette shapes are composed of predominantly platelike polycrystals, mixed-habit rosettes, and rosettes with side plane. Field observations of rosette-shaped ice particles in the temperature range from −40° to −55°C are mostly pristine bullet rosettes. These observations are in agreement with the laboratory findings of Bailey and Hallett (2004).

The particles in cirrus clouds tend to fall into crystal habit categories that are a function of particle size. This is demonstrated in Fig. 5, where the average mass PSD is delineated to show particle habits classified from all of the nine legs flown in the 24 November 2003 deep cirrus cloud. Here we have included small particles to show how spheroids dominate the PSD for sizes <30 μm. From approximately 30 to 150 μm, small irregulars contribute most of the mass. Columns account for only a few percent of the mass and occur mainly in the size range from 25 to 200 μm. Budding rosettes account for approximately 25%–40% of the mass in the size range from 75 to 300 μm and rosette shapes dominate the PSD at sizes of 300 μm and larger. Budding rosettes and rosette shapes account for more than 80% of the mass of cirrus crystals larger than 200 μm in size.

As shown in Fig. 3, the automatic particle habit classification scheme indicates that rosette shapes constitute more than half of the surface area and mass of cirrus particles >50 μm. The data also show that the percentage contribution of rosette shapes increases with increasing temperature. Increasing temperature corresponds with increasing particle size, as shown in Fig. 2. The mass percentages of rosette shapes increase

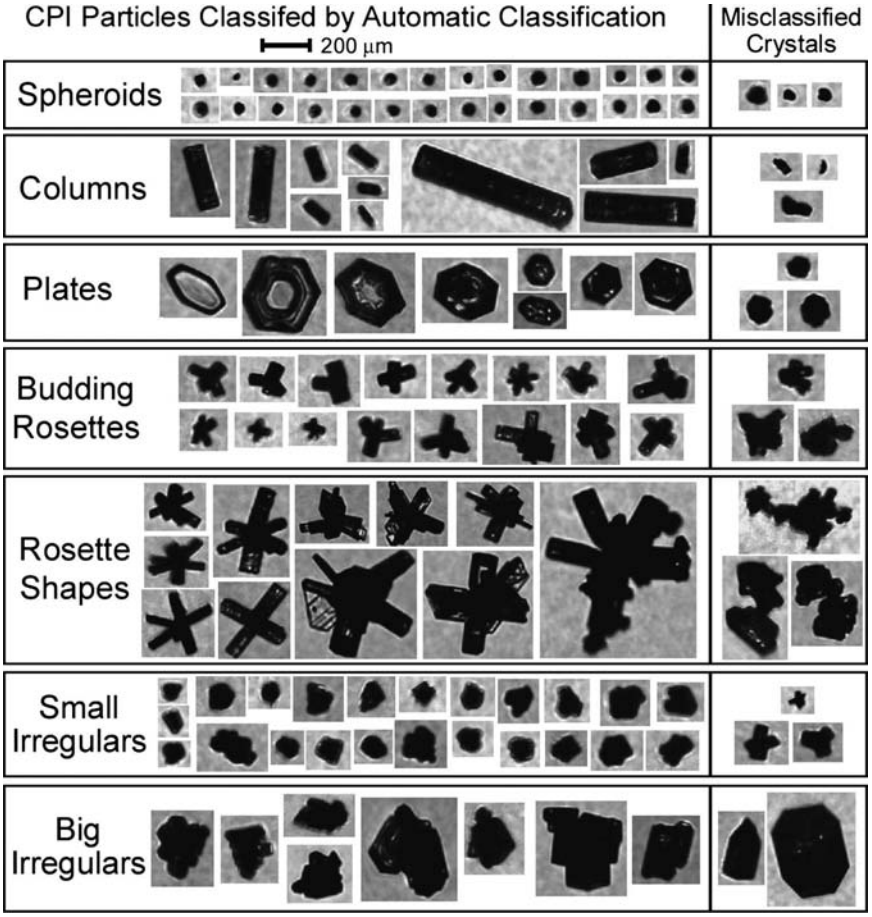

FIG. 4. Examples of CPI particle images from the six categories used in the automatic particle habit classification. Also shown, at right, are examples in each category of particles that have been misclassified.

from approximately 40% at −50°C, to 55% at −40°C, to 80% at −30°C. The trend in the surface area percentages is similar, except that the values are approximately 3% less than the mass values. Irregulars constitute the next largest fraction of particle habits, accounting for approximately 40% of the mass of crystals larger than 50 μm. Small and large irregulars display a habit trend with height that is the opposite of rosette-shaped particles. Small irregulars decrease from approximately 50% at −50°C, to 40% at −40°C, to 15% at −30°C. Thus, the trend for irregulars to decrease with increasing temperature may be due, in part anyway, to the realization that the larger the image, the easier it is to classify (both manually and automatically). It should be noted that columns and spheroidal shapes account for only a few percent each of cirrus particles >50 μm in size; plates are even rarer.

While the habit classification has been restricted to particles with sizes >50 μm, it can be seen from Fig. 2 that particles with sizes <50 μm still contribute significantly to number concentration, area, and mass. Based on data collected in 22 midlatitude cirrus clouds, 99% of the total number of particles, 69% of the extinction, and 40% of the mass comprised particles ≤50 μm. In

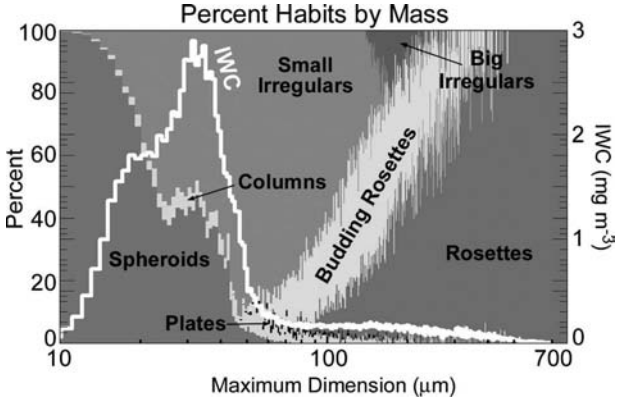

FIG. 5. Mass PSD showing particle habits as a function of particle size for the entire cirrus flight on 24 November 2003.

comparison, Part I found that 99% of the total number of particles, 68% of the extinction, and 38% of the mass comprised particles ≤ 50 μm in wave clouds. A visual inspection of the CPI images with sizes ≤ 50 μm in both wave and cirrus clouds suggests that these are almost always spheroidal particles with no definitive crystal shape, with the caveat that sometimes a faceted crystalline shape (e.g., a small plate) may not be discernable. However, we expect that the actual occurrence of small plates is infrequent since observations of larger plates are rare.

HM95 show balloon replicator measurements of one ascent in a long-lived, large-scale cirrus layer. They also show general results from replicator ascents in five additional cirrus cases and some measurements from horizontal legs flown by the NCAR King Air. The vertical profiles of particle images and aircraft measurements in a few deep cirrus cases, although very limited in scope, offer an opportunity to compare with the more comprehensive measurements presented in this paper. Some results from HM95 are similar to those observed in our work, while others contrast with the results that we present. As mentioned above, HM95 show bimodal PSDs throughout the cirrus layer, and the images show a mixture of rosette shapes, irregular shapes, and small quasi-spheroidal particles, which is in general agreement with our results. However, HM95 report ice particle concentrations that are one to two orders of magnitude less than reported here. This can possibly be explained because HM95 make no correction for collection efficiency in the balloon measurements and they do not include the FSSP measurements from the King Air. HM95 also report that the deep cirrus clouds have a definite structure with a generation region near cloud top with the highest concentration of small particles, an ice-saturated region below that supports particle growth, and a lower region where ice particles sublimate. Their results are largely based on humidity measurements and a numerical model.

The measurements presented in this paper occasionally support the conceptual model presented by HM95 but, for the most part, our measurements show that cirrus clouds are much more complex than suggested by the HM95 model. For example, while our measurements sometimes show the existence of small quasi-spherical particles and budding rosettes near cloud top, in other clouds, the measurements show large, growing rosette shapes near cloud top. Although relative humidity is an obvious factor influencing particle development (HM95), of the parameters measured in our research (relative humidity was not measured), cloud temperature and cloud thickness are most influential in distinguishing ice particle characteristics. Figure 6 shows examples of CPI images of ice particles in regions at the top, middle, and base of clouds. The images have been chosen to emphasize the lack of consistency in particle habits as a function of position in cloud. However, we need to point out that these are not isolated images, or isolated examples, but instead represent the diversity in particle types that can be found in large regions of some clouds. For example, a thin (1 km) cirrus with cloud top at -43°C contains 200–300-μm rosette shapes and another thin cirrus cloud top contains 100–200-μm sublimated ice at -39°C, while a 2-km-thick cirrus shows small ice and budding rosettes at cloud top (-53°C), similar to the HM95 measurements. The examples of particles in Fig. 6 show that particles ranging from small ice to faceted, and growing particles to sublimated ice can be found in midcloud regions. Similarly, large regions with most any particle shape can be found near cloud top and cloud base.

The particle images in Fig. 6 suggest that distance from cirrus cloud top and/or base is not always a good indicator of particle size and shape. Based on relative humidity measurements at temperatures below -30°C, HM95 observed regions of clear air with peak ice supersaturations of up to 20%, suggesting that higher relative humidities may be associated with ice initiation. Figure 6 shows that small particles and crystals with sharp edges can be found throughout the depth of cirrus clouds, suggesting that new ice particles nucleate and can grow at all levels. Similarly, sublimated ice particles can also be found at any location within cloud. The observation that new and growing particles, as well sublimating particles, can be found at all cloud locations is likely reflective of the layer variability in relative humidity often seen in radiosonde observations. When averaged over all clouds (Fig. 3), there are more spheroids and small irregulars at -50°C and more rosette shapes and big irregulars near -30°C. Thus, the HM95 model may be more applicable in a general sense for an average of cirrus clouds where cloud top and cloud base roughly correspond with these temperatures.

While Fig. 6 shows that both growing and sublimating particles can be found at all locations in cirrus clouds, dependent on cloud temperature and cloud depth as well as relative humidity (HM95), an examination of cirrus clouds with thickness ≥ 5000 ft (1.5 km) shows that PSDs in the upper and lower portions of clouds are mostly similar. Figure 7 shows PSDs as a function of number and mass for the cirrus clouds in Table 1 that have a cloud thickness ≥ 5000 ft (1.5 km), divided into upper cloud regions and lower cloud regions. If the cloud is thicker than 8000 ft (2.4 km), then

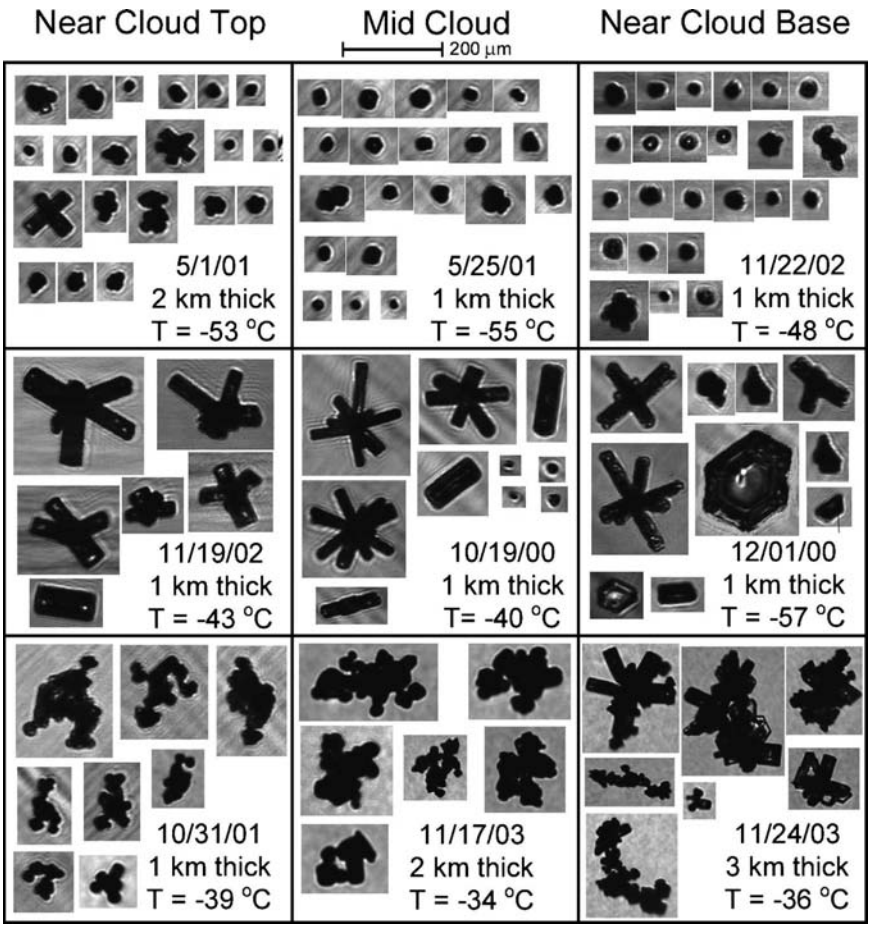

FIG. 6. Examples of CPI images showing the diversity of particle shapes observed near cloud top, midcloud, and near cloud base. Example images were not observed in isolated pockets, but instead in larger regions, sometimes extending the entire length of the cloud pass. Date, observation temperature, and cloud depth are shown for each set of example images.

the upper region is confined to the upper 4000 ft (1.2 km) and the lower region to the lower 4000 ft; otherwise the upper and lower regions are determined by dividing the cloud halfway between cloud top and cloud base. The upper cloud region included measurements from −39° to −57°C and the lower cloud region included measurements from −33° to −46°C. Figure 7 shows that there are only small differences in the average PSDs in the upper portions of cirrus clouds compared with the lower portions. There is slightly more mass in the lower portion, found mostly in the slightly larger tail of the lower-region average PSD. A slightly larger concentration of small ice particles is found in the lower portions of cloud compared with the upper portions of cirrus cloud.

Thus, for relatively thick cirrus clouds, there are only slight differences in the average PSDs from the upper and lower 4000 ft (1.2 km) of cloud. However, as shown in Fig. 6, regions of growing and sublimating particles can be found at all levels in cirrus clouds. Interestingly, examination of Fig. 13 in HM95 is supportive of Fig. 6, as there is very little difference in the ice particle images at cloud top (panel a) and cloud base (panel g) seen in HM95's Fig. 13. By and large, our observations show that the microphysical structure of cirrus clouds is much more diverse and complex than in the HM95 model, which suggests a generalized picture with a generation region near cloud top, growth in midcloud, and sublimation near cloud base.

The similarity in PSDs between deep cirrus clouds and wave clouds is particularly interesting. In wave clouds, Part I separated the average PSDs into two temperature regions, −20° to −37°C and −38 to −60°C. The shapes of the average PSDs in the colder region of wave clouds (Part I) and the average PSD in the region from −50° to −63°C in cirrus (Fig. 2) are very similar. Also, both the average PSDs in the wave cloud region warmer than −37°C and the cirrus cloud region from

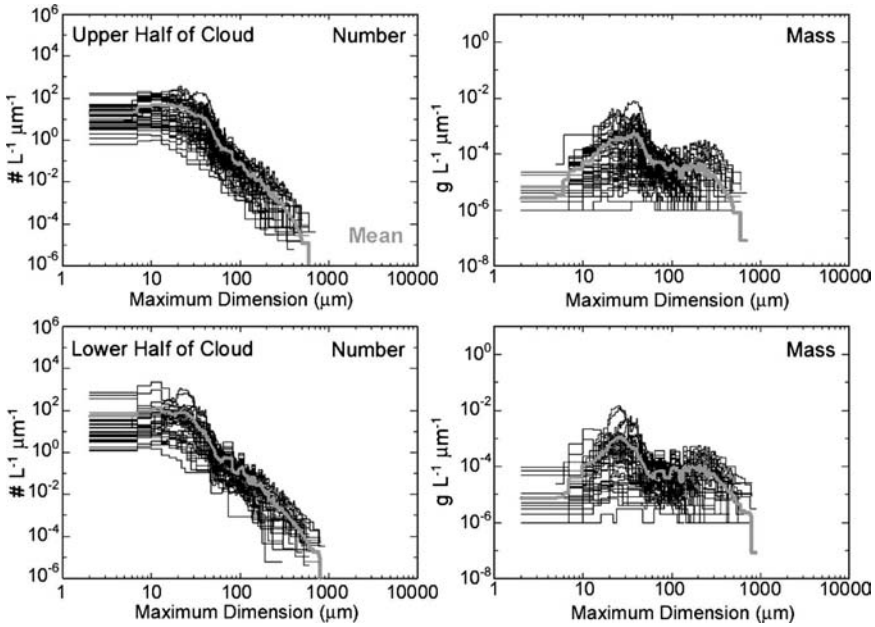

FIG. 7. Number and mass PSDs for upper and lower portions of cirrus clouds with depths ≥5000 ft (1.5 km). If the cloud depth is >8000 ft (2.4 km) the upper and lower portions represent the upper and lower 4000 ft (1.2 km), respectively. If the cloud depth is ≤4000 ft (1.2 km), the upper and lower regions represent the upper and lower halves of the cloud.

−30° to −39°C are strongly bimodal, and the overall shapes of the average PSDs are very similar.

The observations presented here—that is, the strong similarity between wave and cirrus cloud average PSDs, the similarity in percentages of crystal habits (including small spheroidal particles <50 μm), and similar wave cloud and cirrus percentages of concentration, area, and mass of particles <50 μm—lend credence to the (HM95) hypothesis that wave and cirrus clouds experience similar microphysical processes. That is to say, the ice formation process in cirrus may proceed in a way similar to that observed in wave clouds, via freezing of supercooled water and/or solution drops, albeit, at different spatial and temporal scales. The finding that the large majority of the number concentration and area of cirrus particles are spheroidal with sizes ≤50 μm is also important for modeling and studies of radiative transfer (Ivanova et al. 2001).

b. High concentrations of small particles in cirrus

Field et al. (2003) analyzed the interarrival times of particles in cirrus measured by a fast FSSP (Brenguier et al. 1998). From these data they derived a statistic that expressed the degree of departure from the expected Poisson spatial distribution of particles in cloud. Field et al. found that clustering of small particles resulted in a non-Poisson particle distribution. The small particle clustering was associated with relatively high concentrations of 2D-C imaged particles with maximum dimensions >350 μm. They conducted an analysis of the arrival times of the small particles that suggested that the clustering was, at least in part, due to shattering of the large ice particles on the inlet of the FSSP. The measurements reported by Field et al. suggest that the maximum natural ice particle concentration in the cirrus clouds they investigated is on the order of 1 cm^{-3}. Here we examine particle concentrations and related measurements in two cirrus clouds where the maximum particle size did not exceed 100 μm, so that shattering was highly unlikely, while the FSSP ice particle concentration ranged from 2 to 8 cm^{-3}.

On 22 and 23 November 2002 the SPEC Learjet flew coordinated flights with a *Proteus* research aircraft operated by the Sandia National Laboratories under contract to the U.S. Department of Energy. Both flights were flown in thin cirrus in the vicinity of eastern Colorado, western Kansas, and northwestern Okalahoma. In each case, the cirrus deck extended from approximately 33 000 to 35 000 ft, with occasional higher tops (wisps) to approximately 37 000. Both cloud decks had an average cloud-base temperature of −45°C and a cloud-top temperature of −54°C (at 35 000 ft MSL).

From 2335:30 to 2338:30 UTC the Learjet made a gentle climb from 33 600 ft MSL ($T = -50$°C) to 34 700 ft MSL ($T = -52$°C), which was just below cloud top. There was no image activity on the 2D-C probe during

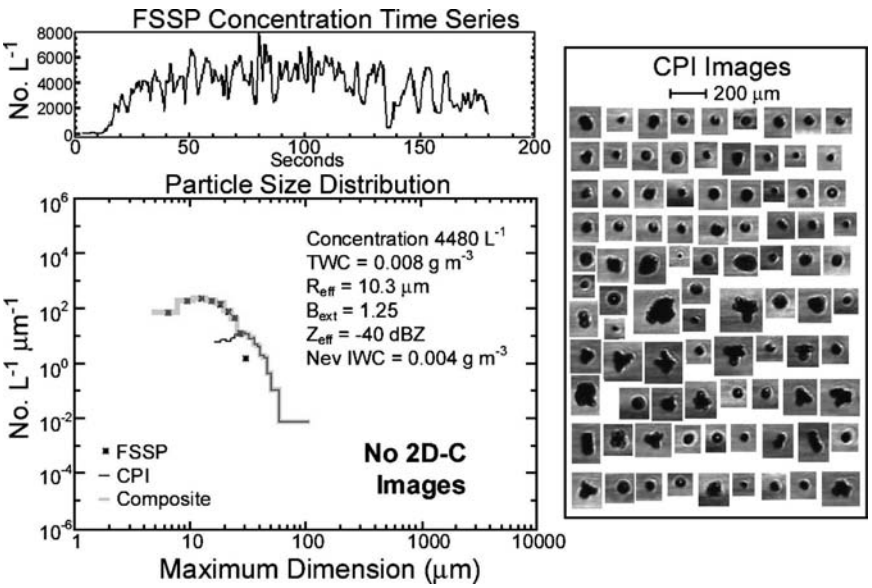

FIG. 8. Learjet data from flight in a thin cirrus cloud on 22 November 2002 showing example of high concentrations of ice where there were no particles detected that were >100 μm. Particle concentration, IWC, effective radius (R_{eff}), and equivalent radar reflectivity (Z_{eff}) are derived from combined FSSP and CPI PSDs and are averaged over the time period from 2336 to 2338 UTC. "Nev IWC" is derived from a Nevzorov total water content sensor.

this time period. The CPI imaged over 1000 particles in the 2-min period. All of the particles were smaller than 100 μm. The lack of activity on the 2D-C probe is not unexpected because at the airspeed of the Learjet, 165 m s^{-1}, the time response of the 2D-C will limit it from imaging particles $<\sim$150 μm (Strapp et al. 2001; Lawson et al. 2006b). There was some very slight activity ($\sim$0.1 L^{-1}) on the 2D-C shadow-or signal, which counts whenever any of its photodiodes is occulted, but this signal cannot be distinguished from noise. Generally, light shadow-or activity in the absence of images occurs when there are particles, but they are too small to produce images. Therefore, it is unlikely that particles >100 μm existed in the flight path of the Learjet, so based on the statistics presented by Field et al. (2003) this is a case where crystal shattering should not enhance ice particle concentration.

Figure 8 shows time series plots of FSSP concentration; a composite FSSP, CPI, and 2D-C PSD; sample CPI images; and derived parameters from one of the two cirrus missions. The time period shown in Fig. 8 is from 2335:30 to 2338:30 UTC 22 November 2002; measurements from the second cirrus mission flown on 23 November 2002 were similar but are not shown here for brevity. The FSSP concentration peaks at approximately 8 cm^{-3} in the middle of the time series plot in Fig. 8. The average ice particle concentration from 2336:00 to 2338:00, a distance of approximately 20 km, is 4.5 cm^{-3}. This is a region with the highest ice particle concentrations observed in this cirrus cloud, although there were other similar periods where concentrations occasionally exceeded 5 cm^{-3}. The high concentrations of small particles cannot be explained by crystal shattering. The CPI images show that most of the particles were small spheroidal shapes, irregulars, and small budding rosettes. The cirrus cloud mission on 23 November 2002 resulted in measurements where concentrations of small particles exceeded 1 cm^{-3} for over 20 km and there were no particles >100 μm.

c. Comparisons to microphysics of wave clouds

Next, in situ Learjet measurements in deep wave clouds and deep cirrus clouds are compared. These results are presented to show the striking similarity in some of the microphysical properties of deep wave clouds and deep cirrus clouds. The main point that will be put forth is that, even though the ice formation process is observable in wave clouds and it is not in cirrus, once ice forms, grows, and then sublimates, the shapes and sizes of the ice crystals are very similar in both types of clouds. This may imply that the predominant nucleation process in wave clouds, immersion freezing of droplets and solution droplets, is also occurring in cirrus clouds, even though it is more difficult to observe.

Part I show PSDs and histograms of particle types for wave clouds in a similar format to Figs. 2 and 3 shown here for cirrus clouds. The shapes of the PSDs in wave

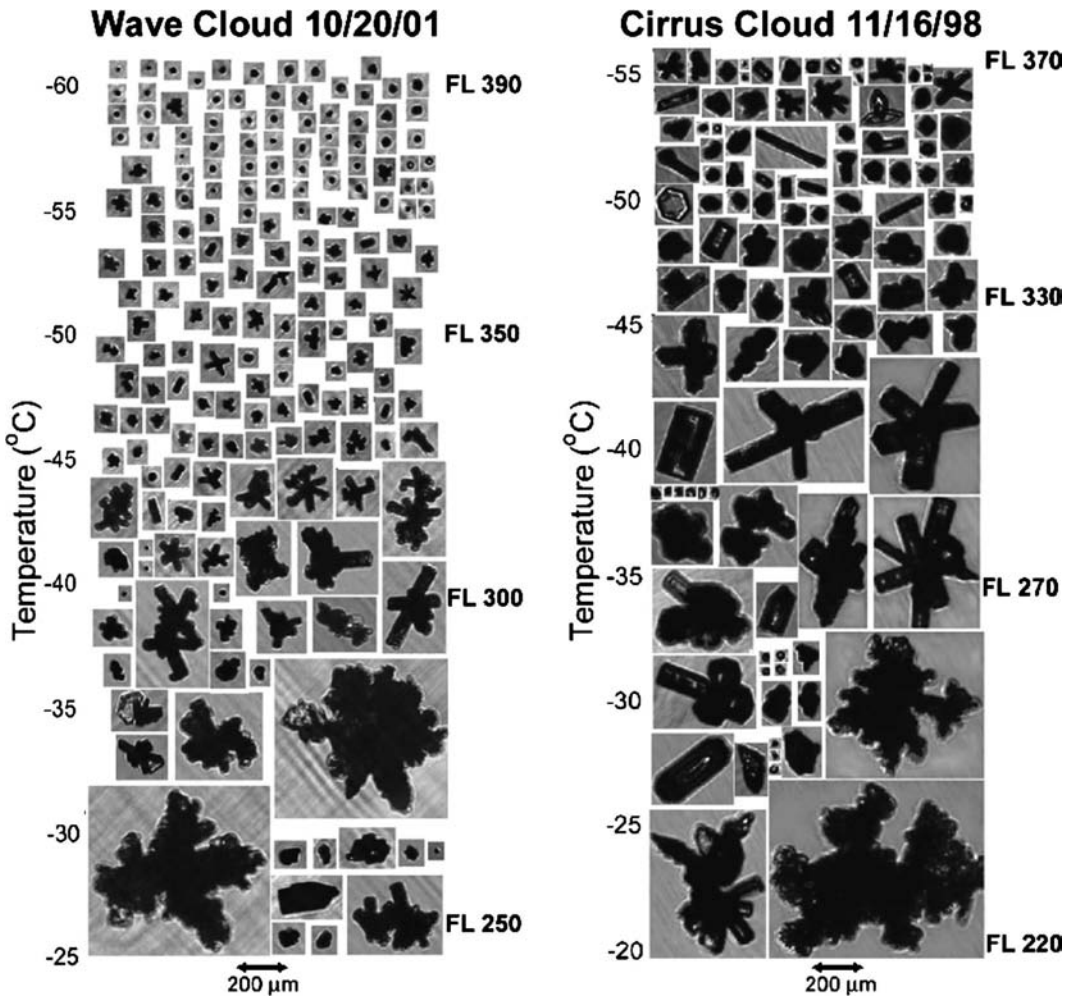

FIG. 9. Comparison of vertical profiles of representative CPI particle images in (left) a wave cloud in the glaciated region just downwind of the location where supercooled liquid water ends and (right) a deep cirrus cloud.

and cirrus clouds show similar tendencies with temperature. That is, the bimodal shape of the average wave cloud mass PSD in the region from −20° to −37°C is very similar to the shape of the average cirrus mass PSD in the region from −30° to −39°C. The average PSD in the region from −38° to −60°C in wave clouds is monomodal, although one of the individual PSDs is bimodal. The average cirrus PSD in the region from −51° to −61°C is nearly monomodal, with only a hint of bimodality, and is thus very similar to the cold temperature region in wave clouds.

The particle sizes in each temperature zone are generally of the same order as those found in the corresponding temperature zone in wave clouds. In both cirrus and wave clouds, the particle size increases with decreasing altitude. As in the wave clouds, small particles $<\sim 50$ μm dominant the number concentration in cirrus clouds. The predominant recognizable particle type >50 μm in both wave clouds and cirrus is the bullet rosette shape with only a few percent columns and $<\sim 1\%$ plates, when the measurements are weighted by mass. Irregular particle shapes are common in both cloud types, accounting for approximately 50% of the mass of the particles at lower ($<\sim -40$°C) temperatures, and $<\sim 25\%$ of the mass at higher ($>\sim -40$°C) temperatures.

Figure 9 shows a comparison of vertical profiles of typical CPI images in a deep cirrus cloud and the glaciated region of a deep wave cloud downwind of the supercooled liquid water region where ice forms. The similarity in the particle types in the deep wave and cirrus clouds is readily apparent. A table showing average measurements in wave clouds at the location just downwind of where the supercooled liquid water ends is shown in Part I. The main difference in average measurements in this region of wave clouds and cirrus

clouds (Table 2) is that the values of particle concentration, IWC, and extinction are roughly an order of magnitude greater in wave clouds than in cirrus clouds. However, in the far-downwind region of wave clouds at approximately −30°C, data presented in Part I show that particle concentration, IWC, and extinction are about the same as in cirrus clouds for this same temperature region. In addition to the visual similarity in particle types, observations of side-plane growth in both wave clouds and deep cirrus clouds suggest that the ice crystal formation processes in both cloud types is similar. CPI images of side planes have also been observed in cirrus clouds by other investigators (e.g., Heymsfield et al. 2002), so this is not a unique occurrence. Part I found, from a careful examination of CPI images in wave clouds, that side planes were rarely observed on crystals that had not exceeded their riming threshold size. This suggests that side-plane growth occurs from subsequent vapor deposition at a riming site.

Part I show measurements in wave clouds indicating that rosette shapes and other polycrystals form in the temperature range from approximately −28° to −55°C. Since polycrystalline structures can result from rapid freezing of supercooled drops at low temperature (Pruppacher and Klett 1997; Bacon et al. 2003), and −37°C is the observed homogeneous freezing point of pure water in the atmosphere, the formation of rosette shapes at temperatures <-37°C suggests that they could be forming on small solution drops or that deposition nucleation on aerosols can also lead to polycrystalline particles. The existence of crystals with side planes in cirrus, which Part I suggest grow at a riming site, also supports the premise that the rosette-shaped particles in cirrus clouds are formed on very small, supercooled liquid and/or solution drops. If the rosette-shaped particles are forming on frozen solution drops, the drops must be very small because detection of supercooled liquid water and aircraft icing are rarely, if ever, observed in cirrus. That is, very small droplets would tend to flow around an airframe and, if droplet impact on the airframe did occur, the potential mass that could be accreted is very small and may not be noticeable. Therefore, the presence of cloud-sized supercooled drops in cirrus is unlikely, or the drops exist only briefly. The similarity in shapes of the PSDs in wave and cirrus clouds suggests that there is a transition from vapor to liquid to ice in both wave and cirrus clouds. The bump in the PSDs at small sizes in wave clouds is attributed to small quasi-spheroidal ice that occurs from freezing of supercooled water and/or solution drops (Part I). A similar bump in the PSDs of cirrus clouds suggests that the ice may also have formed on small water and/or solution drops. The possibility also exists that the nucleation process is the result of deposition; however, we have no evidence to support or refute this possibility.

As discussed above, similarities in the microphysical characteristics of particle formation suggest that the ice in cirrus and wave clouds may be undergoing similar microphysical processes. However, the microphysics of particle nucleation and growth can be observed more readily in wave clouds because the process occurs more quickly as air flows through the nearly stationary cloud. Also, the updraft velocities in wave clouds are sustained and much larger (cf. Heymsfield and Miloshevich 1993 with Ström 2004), so cloud drops in wave clouds are generated in a more predictable and prolific manner. In cirrus clouds the conversion of cloud condensation nuclei to cloud drops is difficult to observe. This is because it is logistically difficult to place research aircraft in the formation stage of cirrus clouds and the extents of the updrafts are small. Thus, generally any solution or cloud drops that are generated in cirrus will be very tiny, and only the end products (i.e., ice crystals) are typically observed. The data presented here suggest that the ice particles in cirrus clouds first go through a conversion from water vapor to liquid and solution droplets, which freeze at low ($<\sim-30$°C) temperatures, thereby developing polycrystalline ice particles through a microphysical process that may be similar to wave clouds.

d. Dimensional properties of ice particles

Cirrus clouds are a critical component in the earth's radiation budget (Liou 1986) and the radiative properties of cirrus are strongly dependent on particle size and shape (Stephens et al. 1990; Mishchenko et al. 1996). In this section, we examine a geometric relationship, plots of particle area to length, and compare this relationship to area-to-length plots of particles in wave clouds. Figure 10 shows area-to-length relationships for rosette shapes and budding rosettes, columns, irregulars, and all particles >50 μm based on 104 legs in the 22 cirrus clouds. As expected, the columns have the smallest area-to-length ratio, followed by rosette shapes and then irregulars. The best-fit least squares equations for the area-to-length relationship in cirrus are shown in Fig. 10 and can be used for radiation studies. Figure 11 shows area-to-length relationships as a function of temperature for all particles >50 μm in the 22 cirrus clouds on a log–log plot, shows a trend whereby the area-to-length ratios of ice particles increase with increasing temperature. This trend results from the increase in side-plane, complex shapes and irregulars found lower in thick cirrus clouds at higher temperatures (see Fig. 9).

Figure 12 shows a comparison of particle area-to-

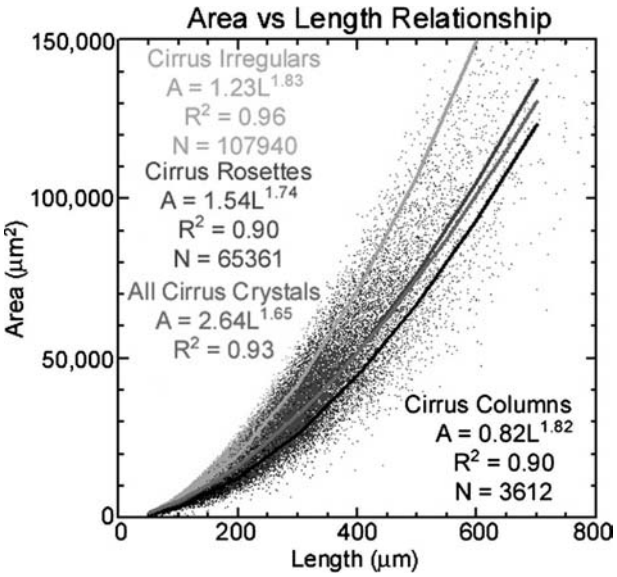

FIG. 10. Plot of CPI image projected area vs length for columnar, rosette shapes, irregular, and all-ice particles >50 μm in 22 cirrus clouds listed in Table 1. Best-fit least squares equations and correlation coefficients are shown for each curve.

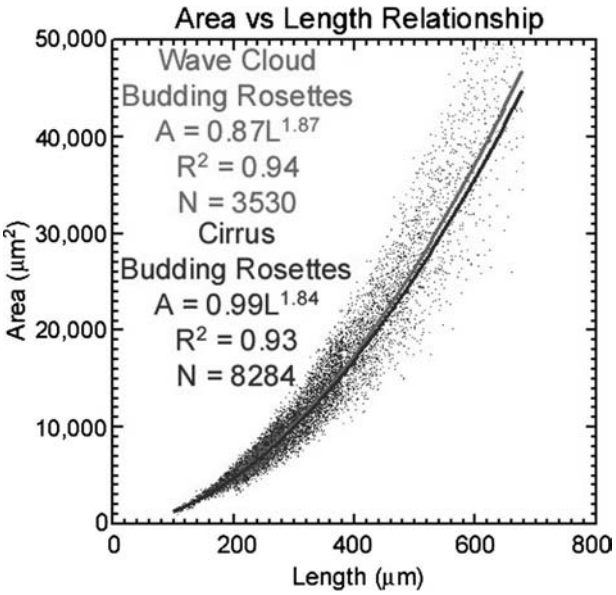

FIG. 12. As in Fig. 10 except data show comparison of budding rosettes in the regions of wave clouds and cirrus clouds with temperatures $<-37°$C.

length relationships for budding rosettes in wave clouds and cirrus clouds at temperatures $<-37°$C. The low temperature range was selected to isolate crystals that did not contain side planes and riming. The comparison does not reveal any detectable differences between budding rosettes in cirrus and wave clouds at temperatures below $-37°$C. On the other hand, Fig. 13 shows a comparison of the geometries of rosette shapes and budding rosettes, at all temperatures in wave and cirrus clouds. For purposes of comparison, we also show in Fig. 13 a typical curve for chainlike aggregates that are often observed in the anvils of continental thunderstorms (Connolly et al. 2005). The chainlike aggregates

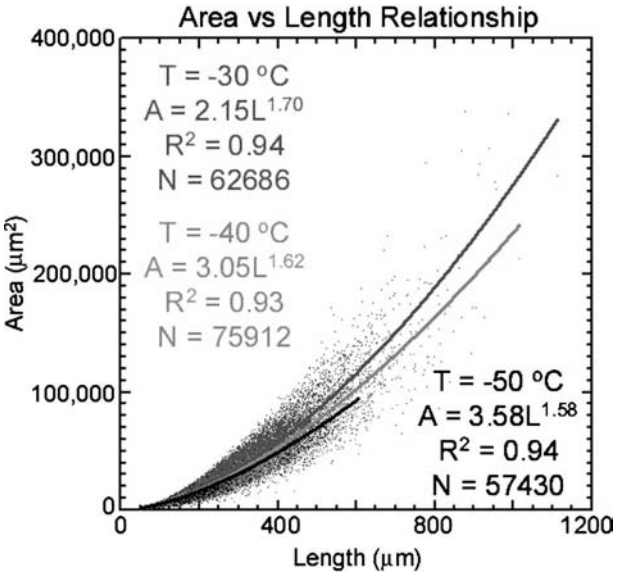

FIG. 11. Log–log plot showing particle area vs particle length as a function of temperature for all particles >50 μm in the 22 cirrus clouds shown in Table 1.

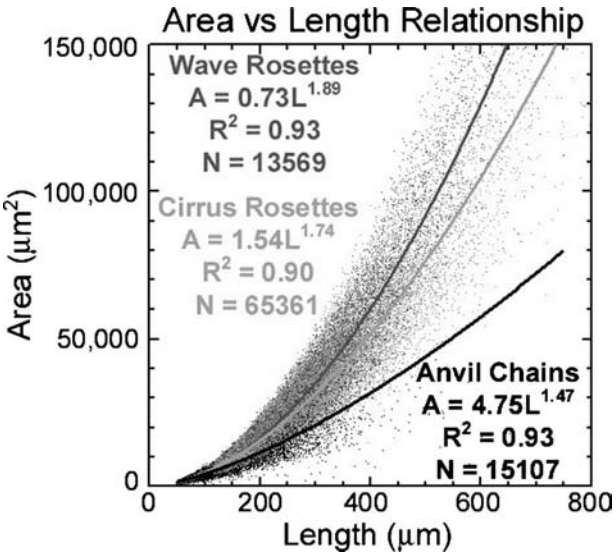

FIG. 13. As in Fig. 12 except data are for rosette shapes and budding rosettes at all temperatures in wave clouds and cirrus clouds. Chainlike particles, which appear as chains of small ice particles in anvils (Connolly et al. 2005), are shown to emphasize the difference in the geometric relationship of this particle shape.

generally have aspect ratios >2:1 and thus are expected to have substantially smaller area-to-length ratios. The comparison in Fig. 13 is shown to provide a comparison of the magnitude of the difference in area-to-length ratios that can be expected in cirrus and anvil clouds.

The data show that wave cloud particles tend to have slightly larger area-to-length ratios than particles in cirrus clouds. Based on visual inspection of CPI images in both wave and cirrus clouds, we attribute this to the overall increased amount of riming and side-plane growth in the wave cloud dataset. The increased riming and side plane is attached to the side of the branches on rosette-shaped particles; when viewed as a two-dimensional projection, this effectively fills in the clear space between the arms of rosette-shaped particles. The increased riming and side-plane growth in wave clouds is expected because supercooled liquid water is frequently observed in the wave cloud dataset.

4. Summary and discussion

Microphysical measurements were collected during 22 Learjet missions flown in midlatitude cirrus. The dataset was collected while the aircraft flew 104 horizontal legs, totaling over 15 000 km in cloud. Temperatures ranged from −28° to −61°C; however, the majority of the data were collected between temperatures from approximately −35° to −50°C. This is the most comprehensive dataset yet collected of CPI measurements of midlatitude cirrus particle sizes and shapes.

The measurements show that cirrus particle size distributions (PSDs) are bimodal, displaying a maximum in number concentration, area, and mass near 30 μm and another smaller maximum near 200–300 μm, similar in shape to those reported by Ivanova (2001). Particles with rosette shapes, which include budding rosettes with short arms, mixed-habit rosettes, rosettes with side planes, and platelike polycrystals constitute over 50% of the surface area and mass of ice particles >50 μm in cirrus clouds. Approximately 40% of the remaining mass of ice particles >50 μm is found in irregular shapes, with a few percent each in columns and spheroidal shapes. Plates account for <1% of the total mass in these midlatitude cirrus. Particles <50 μm account for 99% of the total number concentration, 69% of the extinction, and 40% of the mass in midlatitude cirrus. The relatively high percentage of rosette shapes and low percentages of columns and plates differs somewhat from datasets collected using older measurement technologies, which suggested that spatial polycrystals, columns, and plates were predominant (e.g., Heymsfield and Platt 1984; Dowling and Radke 1990). However, the spatial polycrystals observed on an impactor by Heymsfield and Platt are similar in appearance to the rosette shapes observed in our work.

The average particle concentration in cirrus is on the order of 1 cm^{-3}. The highest concentrations (>5 cm^{-3}) are typically found in the lower parts of deep (>3 km) cirrus clouds, although there are some instances where these high concentrations were observed in thin cirrus. These values of particle concentration are considerably higher than earlier estimates, which were on the order of 0.01–0.1 cm^{-3} (Heymsfield and Platt 1984; Dowling and Radke 1990). However, the higher concentrations reported here are in general agreement with later estimates (Lawson et al. 2001; Gayet et al. 2002; Field et al. 2003). There is some question of actual particle concentration due to the potential contribution of particle shattering on probe inlets (Field et al. 2003). We show examples of measurements in cirrus where there are no particles >100 μm (well below the minimum size thought to contribute to particle shattering), and concentrations in these cirrus range from 3 to 8 cm^{-3} averaged over several kilometers. Thus, the data suggest that, while crystal shattering may inflate the number of small particles in some cirrus clouds, there are instances where crystal shattering is highly unlikely and very high concentrations of small particles are still observed.

The resemblance of microphysical properties of ice particles in wave clouds (Part I) and cirrus clouds may not be coincidental. There is definite similarity in the shapes of the PSDs with a maximum near approximately 30 μm. Crystal habits are similar in both cirrus and wave clouds, as are observations of side planes, which Part I suggest is correlated with growth at a riming site. HM95 and Part I show that the formation of ice particles in wave clouds follows the conversion of water vapor to cloud and/or solution drops at temperatures above −37°C, and possibly from vapor to tiny solution drops at temperatures below −37°C. Under these conditions, immersion freezing or possibly "inside–out contact nucleation" (Shaw et al. 2005; Part I) occurs at temperatures above −37°C, and homogeneous freezing occurs at temperatures below −37°C. The possibility of depositional freezing also exists at temperatures lower than −37°C, but we have no evidence to support this process. The result of immersion freezing and homogeneous freezing is the formation of polycrystalline ice, which often grows into rosette shapes. Based on this circumstantial comparison, the hypothesis can be drawn that ice particles in cirrus clouds also undergo conversion from water vapor to liquid and/or solution drops before freezing to form polycrystalline ice. That is, the cirrus clouds proceed through the same physical processes as wave clouds but on larger spatial and temporal scales.

Acknowledgments. Jay Mace and Ken Sassen of the University of Utah played major roles in forecasting cirrus formation and coordinating the data collection in conjunction with remote ground measurements. We are very grateful to Bill Harris and Cleon Biter for their excellent piloting skills. This work was performed under NSF Grant ATM-0244731, NASA EOS 98-0-3, PO 83511 from the University of Utah, and NASA Grant NNG04E71G.

REFERENCES

Arnott, W. P., Y. Dong, and J. Hallett, 1994: Role of small ice crystals in radiative properties of cirrus: A case study, FIRE II, November 22, 1991. *J. Geophys. Res.,* **99,** 1371–1381.

Bacon, N. J., M. B. Baker, and B. D. Swanson, 2003: Initial stages in the morphological evolution of vapour-grown ice crystals: A laboratory investigation. *Quart. J. Roy. Meteor. Soc.,* **129,** 1903–1927.

Bailey, M., and J. Hallett, 2004: Growth rates and habits of ice crystals between −20° and −70°C. *J. Atmos. Sci.,* **61,** 514–544.

Baker, B. A., and R. P. Lawson, 2006a: In situ observations of the microphysical properties of wave, cirrus, and anvil clouds. Part I: Wave clouds. *J. Atmos. Sci.,* **63,** 3160–3185.

——, and ——, 2006b: Improvement in determination of ice water content from two-dimensional particle imagery. Part I: Image-to-mass relationships. *J. Appl. Meteor. Climatol.,* **45,** 1282–1290.

Brenguier, J.-L., T. Bourrianne, A. de Araujo Coelho, J. Isbert, R. Peytavi, D. Trevarin, and P. Wechsler, 1998: Improvements of droplet size distribution measurements with the fast-FSSP. *J. Atmos. Oceanic Technol.,* **15,** 1077–1090.

Connolly, P. J., C. P. R. Saunders, M. W. Gallagher, K. N. Bower, M. J. Flynn, T. W. Choularton, J. Whiteway, and R. P. Lawson, 2005: Aircraft observations of the influence of electric fields on the aggregation of ice crystals. *Quart. J. Roy. Meteor. Soc.,* **131,** 1695–1712.

Cooper, W. A., and G. Vali, 1981: The origin of ice in mountain cap clouds. *J. Atmos. Sci.,* **38,** 1244–1259.

Cotton, R. J., P. R. Field, O. Field, M. Schnaiter, M. Kraemer, P. Connolly, and A. J. Heymsfield, 2004: Parcel modeling of ice nucleation in the Aida aerosol chamber. *Proc. 14th Int. Conf. on Clouds and Precipitation,* Vol. 1, Bologne, Italy, International Commission of Clouds and Precipitation, 751–755.

Dowling, D. R., and L. F. Radke, 1990: A summary of the physical properties of cirrus clouds. *J. Appl. Meteor.,* **29,** 970–978.

Field, P. R., R. Wood, P. R. A. Brown, P. H. Kaye, E. Hirst, R. Greenaway, and J. A. Smith, 2003: Ice particle interarrival times measured with a fast FSSP. *J. Atmos. Oceanic Technol.,* **20,** 249–261.

——, R. J. Cotton, O. Field, M. Schnaiter, M. Kramer, P. Connoll, and A. J. Heymsfield, 2004: Investigation of the ice nucleation ability of two desert dust aerosol samples at −50°C. *Proc. 14th Int. Conf. on Clouds and Precipitation,* Vol. 1, Bologne, Italy, International Commission of Clouds and Precipitation, 78–81.

Gayet, J.-F., and Coauthors, 2002: Quantitative measurement of the microphysical and optical properties of cirrus clouds with four different in situ probes: Evidence of small ice crystals. *Geophys. Res. Lett.,* **29,** 2230–2233.

Heymsfield, A. J., 1973: Laboratory and field observations of the growth of columnar and plate crystals from frozen droplets. *J. Atmos. Sci.,* **30,** 1650–1656.

——, and C. M. R. Platt, 1984: A parameterization of the particle size spectrum of ice clouds in terms of the ambient temperature and the ice water content. *J. Atmos. Sci.,* **41,** 846–855.

——, and L. M. Miloshevich, 1993: Homogeneous ice nucleation and supercooled liquid water in orographic wave clouds. *J. Atmos. Sci.,* **50,** 2335–2353.

——, and ——, 1995: Relative humidity and temperature influences on cirrus formation and evolution: Observations from wave clouds and FIRE II. *J. Atmos. Sci.,* **52,** 4302–4326.

——, S. Lewis, A. Bansemer, J. Iaquinta, L. M. Miloshevich, M. Kajikawa, C. Twohy, and M. R. Poellot, 2002: A general approach for deriving the properties of cirrus and stratiform ice cloud particles. *J. Atmos. Sci.,* **59,** 3–29.

Ivanova, D., D. L. Mitchell, W. P. Arnott, and M. Poellot, 2001: A GCM parameterization for bimodal size spectra and ice mass removal rates in mid-latitude cirrus clouds. *J. Atmos. Res.,* **59-60,** 89–113.

Kajikawa, M., and A. J. Heymsfield, 1989: Aggregation of ice crystals in cirrus. *J. Atmos. Sci.,* **46,** 3108–3121.

Knollenberg, R. G., 1970: The optical array: An alternative to scattering or extinction for airborne particle size determination. *J. Appl. Meteor.,* **9,** 86–103.

——, 1981: Techniques for probing cloud microstructure. *Clouds Their Formation, Optical Properties, and Effects,* P. V. Hobbs and A. Deepak, Eds., Academic Press, 15–91.

Korolev, A. V., and G. A. Isaac, 2004: Observation of sublimating ice crystals in clouds. *Proc. 14th Int. Conf. on Clouds and Precipitation,* Vol. 1, Bologne, Italy, International Commission of Clouds and Precipitation, 808–811.

——, S. V. Kuznetsov, Y. E. Makarov, and V. S. Novikov, 1991: Evaluation of measurements of particle size and sample area from optical array probes. *J. Atmos. Oceanic Technol.,* **8,** 514–522.

——, J. W. Strapp, and G. A. Isaac, 1998a: Evaluation of the accuracy of PMS optical array probes. *J. Atmos. Oceanic Technol.,* **15,** 708–720.

——, ——, ——, and A. N. Nevzorov, 1998b: The Nevzorov airborne hot-wire LWC–TWC probe: Principle of operation and performance characteristics. *J. Atmos. Oceanic Technol.,* **15,** 1495–1510.

Kristjánsson, J. E., J. M. Edwards, and D. L. Mitchell, 2000: Impact of a new scheme for optical properties of ice crystals on climates of two GCM's. *J. Geophys. Res.,* **105,** 10 063–10 079.

Labonnote, L., G. Brogniez, M. Doutriaux-Boucher, J.-C. Buriez, J.-F. Gayet, and H. Chepfer, 2000: Modeling of light scattering in cirrus clouds with inhomogeneous hexagonal monocrystals: Comparison with in-situ and ADEOS-POLDER measurements. *Geophys. Res. Lett.,* **27,** 113–116.

Lawson, R. P., B. A. Baker, C. G. Schmitt, and T. L. Jensen, 2001: An overview of microphysical properties of Arctic clouds observed in May and July during FIRE ACE. *J. Geophys. Res.,* **106,** 14 989–15 014.

——, ——, P. Zmarzly, D. O'Connor, Q. Mo, J.-F. Gayet, and V. Shcherbakov, 2006a: Microphysical and optical properties of atmospheric ice crystals at South Pole Station. *J. Appl. Meteor. Climatol.,* **45,** 1505–1524.

——, D. O'Connor, P. Zmarzly, K. Weaver, B. A. Baker, Q. Mo, and H. Jonsson, 2006b: The 2D-S (stereo) probe: Design and preliminary tests of a new airborne, high-speed, high-resolution particle imaging probe. *J. Atmos. Oceanic Technol.,* **23,** 1462–1477.

Liou, K. N., 1986: Influence of cirrus clouds on weather and climate processes: A global perspective. *Mon. Wea. Rev.,* **114,** 1167–1199.

Miloshevich, L. M., and A. H. Heymsfield, 1997: A balloon-borne continuous cloud particle replicator for measuring vertical profiles of cloud microphysical properties: Instrument design, performance, and collection efficiency analysis. *J. Atmos. Oceanic Technol.,* **14,** 753–768.

Mishchenko, M. I., W. B. Rossow, A. Macke, and A. A. Lacis, 1996: Sensitivity of cirrus cloud albedo, bidirectional reflectance, and optical thickness retrieval accuracy to ice-particle shape. *J. Geophys. Res.,* **101,** 16 973–16 985.

Mitchell, D. L., R. Zhang, and R. L. Pitter, 1990: Mass-dimensional relationships for ice particles and the influence of riming on snowfall rates. *J. Appl. Meteor.,* **29,** 153–163.

Ohtake, T., and M. Inoue, 1980: Formation mechanism of ice crystal precipitation in the Antarctic atmosphere. Preprints, *Eighth Int. Conf. on Cloud Physics,* Vol. 1, Clermont-Ferrand, France, International Commission of Clouds and Precipitation, 221–224.

Pruppacher, H. R., and J. D. Klett, 1997: *Microphysics of Clouds and Precipitation.* Kluwer Academic, 954 pp.

Sassen, K., J. M. Comstock, Z. Wang, and G. Mace, 2001: Cloud and aerosol research capabilities at FARS: The Facility for Atmospheric Remote Sensing. *Bull. Amer. Meteor. Soc.,* **82,** 1119–1138.

Shaw, R. A., A. J. Durant, and Y. Mi, 2005: Heterogeneous surface crystallization observed in undercooled water. *J. Phys. Chem.,* **109,** 9865–9868.

Stephens, G. L., S.-C. Tsay, P. W. Stackhouse, and P. J. Flatau, 1990: The relevance of the microphysical and radiative properties of cirrus clouds to climate and climatic feedback. *J. Atmos. Sci.,* **47,** 1742–1753.

Strapp, J. W., F. Albers, A. Reuter, A. V. Korolev, U. Maixner, E. Rashke, and Z. Vukovic, 2001: Laboratory measurements of the response of a PMS OAP-2DC. *J. Atmos. Oceanic Technol.,* **18,** 1150–1170.

Ström, J., 2004: Vertical motions at cirrus altitudes. *Proc. 14th Int. Conf. on Clouds and Precipitation,* Vol. 2, Bologne, Italy, International Commission of Clouds and Precipitation, 1750–1753.